



Phase transition of Fe_2O_3 – NiO to NiFe_2O_4 in perovskite catalytic particles for enhanced methane chemical looping reforming-decomposition with CO_2 conversion

Hyun Suk Lim, Dohyung Kang, Jae W. Lee*

Department of Chemical and Biomolecular Engineering, Korea Advanced Institute of Science and Technology (KAIST), Daejeon 305-701, Republic of Korea



ARTICLE INFO

Article history:

Received 10 June 2016

Received in revised form 10 August 2016

Accepted 10 September 2016

Available online 11 September 2016

Keywords:

Phase transition of metal oxide
Chemical looping
Perovskite

ABSTRACT

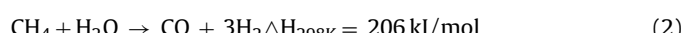
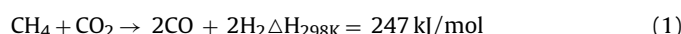
This work introduced a perovskite catalytic particle of Fe_2O_3 – $\text{NiO}/\text{La}_{0.8}\text{Sr}_{0.2}\text{FeO}_3$ as an oxygen carrier and investigated its long-term activity and stability in a novel methane Chemical Looping Reforming-Decomposition (CLRD) process. Carbon dioxide (CO_2) was injected for the oxidation of the reduced catalytic particle and its carbon deposit, resulting in the accelerated production of syngas. The catalytic particle showed over 97% of CH_4 conversion over 60 min and the reduced catalytic particle was partially re-oxidized by both O_2 and CO_2 with the conversion of CO_2 into CO maintaining about 93% over 80 min. The separate phases of Fe_2O_3 / NiO were gradually merged to the single crystal phase of NiFe_2O_4 during the calcination of the two metal oxides and the continuous redox reaction cycle. The increased crystallinity can lead to the improvement of both activity and stability due to the enhanced oxygen-carrying capacity. The structure of the catalytic particle was well preserved and its activity has been stable in the long-term CLRD cycle with the combination of CO_2 utilization.

© 2016 Elsevier B.V. All rights reserved.

1. Introduction

Since crude oils have become depleted and natural gas has been more available due to the discovery of shale gas reservoirs, various studies to produce useful products from natural gas instead of petroleum have been performed on these days [1–3]. Thus, a multi-step conversion route of methane into synthesis gas (syngas) such as hydrogen and carbon monoxide has been developed [4–8] and efficient methods for methane reforming are important because this reforming reaction is both capital and energy intensive.

Three representative pathways to reform methane are steam reforming of methane (SRM) [9–11], dry reforming of methane (DRM) [12–14], and partial oxidation of methane (POM) [15–17]. SRM uses steam to crack methane into syngas and DRM utilizes the reaction of carbon dioxide with methane to produce syngas. These two reforming reactions are as follows;



These two reactions are endothermic and additional energy is required to sustain those reactions. On the other hand, POM uses a small quantity of oxygen to incompletely combust methane and it is an exothermic reaction.



Thus, an auto-thermal process is available since energy required to maintain a high reaction temperature is automatically supplied from the released heat of reaction. Nevertheless, POM has three major drawbacks which hinder its industrial implementation; the flammability issue arises because of mixing methane and oxygen and additional processes are required to separate syngas from nitrogen in air. Also, there is a requirement of noble metal like platinum to act as a catalyst [18].

In order to overcome these drawbacks, chemical looping reforming (CLR) was proposed because oxygen indirectly reacts with methane using metal oxides as a medium of lattice oxygen (O^{2-}) [19–21]. First, CH_4 is partially oxidized by the lattice oxygen from the metal oxide and the metal oxide is fully reduced to the metal form. Consumed lattice oxygens are fully recovered by air in another reactor. Since CH_4 and air are injected without encountering each other, separation processes to recover the produced syngas from the depleted air can be eliminated. A reduction rate of the metal oxides by CH_4 is important in this reaction because the

* Corresponding author.

E-mail address: jaewlee@kaist.ac.kr (J.W. Lee).

rapid reduction of the oxides can lead to the full oxidation of CH₄ and the production of CO₂ and H₂O [19].

Various studies have been conducted to select an efficient metal oxide and improve its activity. Until now, nickel-based oxides have mainly been studied as catalysts and oxygen carriers [22–26] and showed high reactivity toward CH₄ with both high conversion of CH₄ and high thermal stability over 900 °C [18]. The wide use of nickel oxides was still hampered due to their low syngas selectivity [27], relatively high cost, and not environmental-friendly nature [28,29]. Iron-based oxides are cheaper than nickel oxides, so they have widely been studied as an alternative of nickel oxides. However, because iron-based oxides have lower reactivity than nickel oxides, a supporter such as Al₂O₃ and ZrO₂ is required to overcome these drawbacks [30–33]. Luke et al. [34] proposed a core-shell particle of for chemical looping reforming of methane. The perovskite structure enhances activity toward CH₄, with an improved thermal stability over harsh conditions, and controls oxygen mobility from bulk Fe₂O₃ phase to the surface. Thus, the syngas selectivity was maintained high with relatively large ratios of oxygen to methane.

Fe₂O₃–CuO/Al₂O₃ was used as an oxygen carrier for combining Chemical Looping Combustion (CLC) and steam gasification into one process where energy required to gasify coke can be supplied from the exothermic CLC cycle [35]. CH₄ was continuously injected after the complete carrier reduction to have both methane decom-

position (CMD) and coke formation. Steam then entered to the reduced metal and produced additional syngas by reacting with coke (C + H₂O = CO + H₂). After the complete removal of coke, metals are fully recharged with oxygen in air and used again for POM. Likewise, CO₂ can also be utilized in the looping process to produce CO [36–38].

NiFe₂O₄ was employed as an oxygen carrier particle to understand redox behaviors for chemical looping [39,40] and compared its performance with that of pure NiO and Fe₂O₃ [41]. NiFe₂O₄ showed more uniform oxygen desorption than the other two metal oxides and gradual improvement of the redox activity over the repeated cycle. This indicates that NiFe₂O₄ could be a suitable oxygen carrier for the CLR process because a controlled quantity of oxygen transferred for the oxidation of CH₄ can suppress the complete combustion, which leads to the increased selectivity toward syngas with the improved stability.

This work introduces the formation of the single crystal phase of NiFe₂O₄ from mixed iron/nickel oxides in the Fe₂O₃–NiO/La_{0.8}Sr_{0.2}FeO₃ (Fe-Ni/LSF) perovskite catalytic particles. In a proposed methane chemical looping reforming and decomposition (CLRD) process, this study demonstrates the enhanced activity and cycle stability of the particles by having the phase transition from the biphasic Fe₂O₃–NiO to the single crystal-phase of NiFe₂O₄. The transition of the phase and its effect on the redox performance will be captured through microscopic and

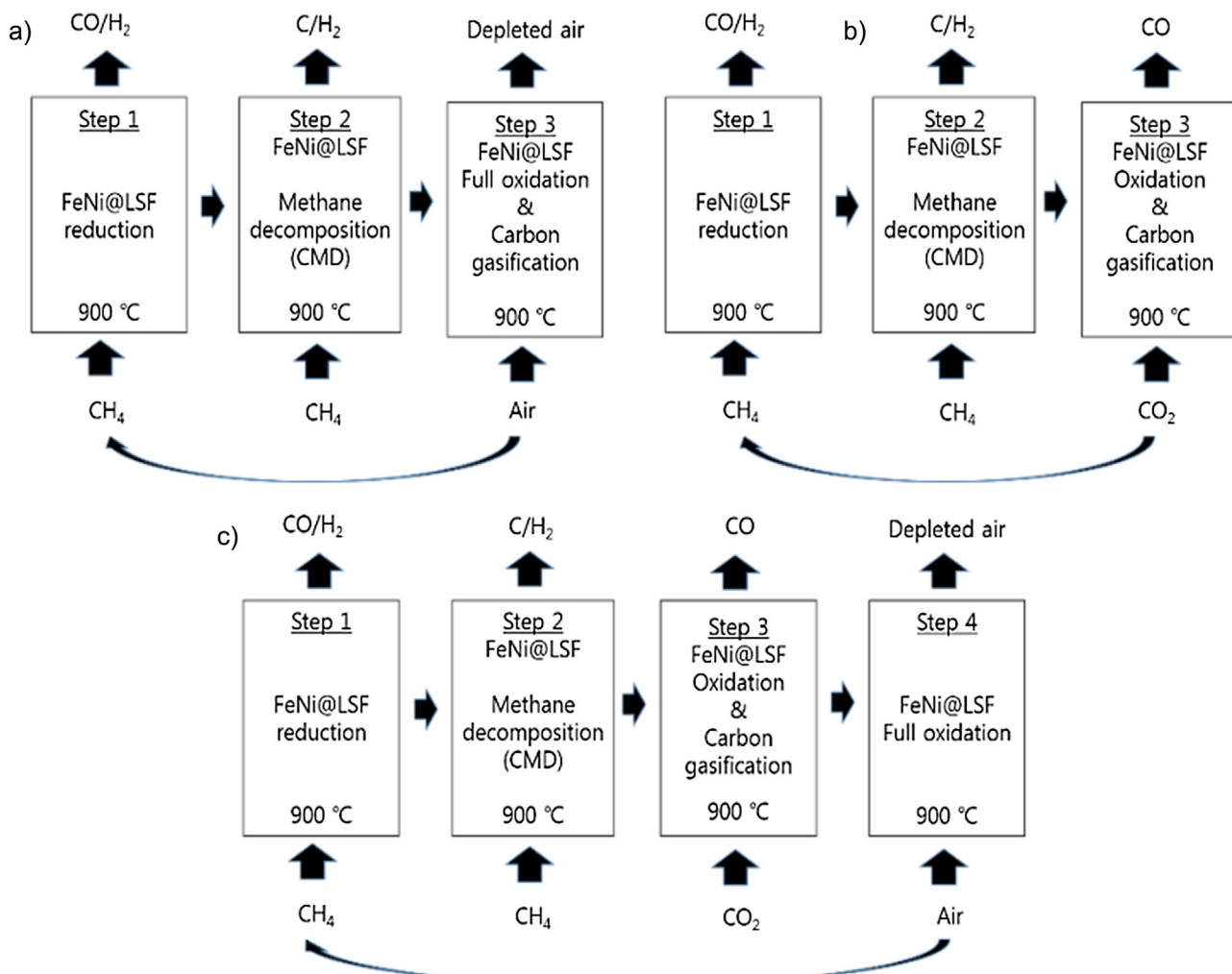


Fig. 1. Scheme of O₂-CLRD process (a), CO₂-CLRD process (b), and comb-CLRD process (c).

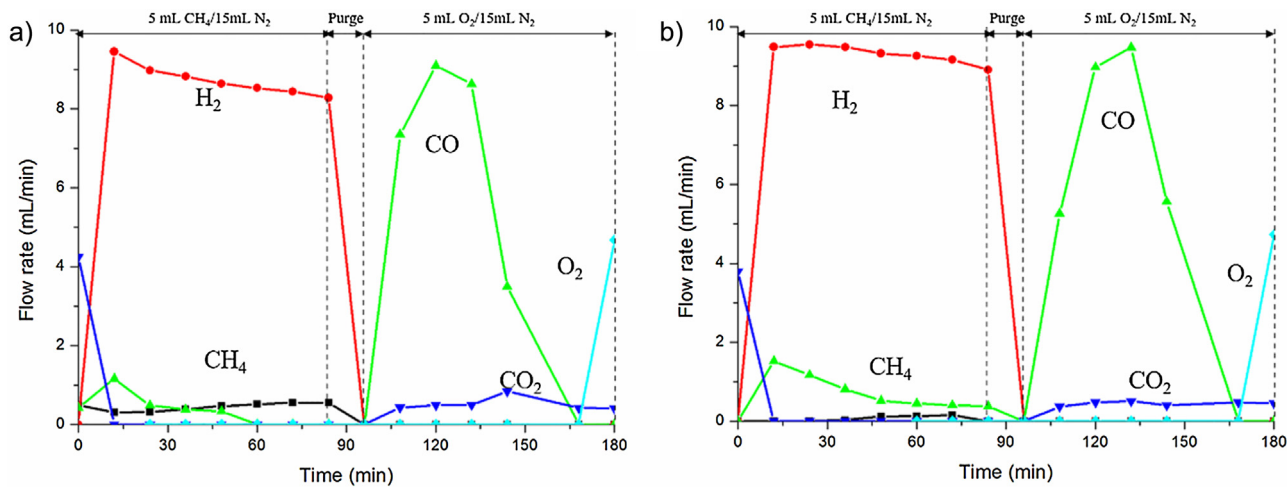


Fig. 2. Gas evolution profiles of O₂-CLRD process with the fresh particle (a) and the 10-cycle spent particle (b).

spectroscopic investigations. In the proposed methane CLRD processes, both catalytic CH₄ decomposition and CO₂ oxidation steps are incorporated between CH₄ reduction and O₂ oxidation steps to increase syngas production from the coke gasification by gaseous CO₂.

It will be shown that a small amount of O₂ is required to fully replenish the lattice oxygen in the catalytic particle oxidation step due to the prior CO₂ oxidation/gasification step. By combining both CH₄ reforming and decomposition with the regeneration of the particles through the coke gasification by CO₂, the production of syngas is highly increased with prolonged cycle operations. The data of X-ray diffraction (XRD) will demonstrate the phase change of the metal oxide from the mixture of Fe₂O₃ and NiO to a single crystal phase of NiFe₂O₄, which will be further confirmed by the H₂ Temperature Programmed Reduction (H₂-TPR). H₂-TPR will also show that the transition to the single crystal phase can enhance oxygen carrying capacity and activate more lattice oxygen to participate in the syngas production. Results from X-ray photoelectron spectroscopy (XPS) and transmission electron microscopy (TEM) will show that the particles might have a stable core-shell structure under the cyclic process.

2. Experimental section

2.1. Preparation of perovskite catalytic particles

A modified Pechini method was used to prepare the redox perovskite catalytic particles. To prepare metal oxide nanoparticles, equimolar Fe₂O₃ (<50 nm, Aldrich) and NiO nanoparticles (<50 nm, Aldrich) were dispersed in 60% ethanol aqueous solution and sonicated for 30 min at room temperature. After settling for 6 h, the upper layer of the solution was separated to remove the excess liquid phase. For the preparation of the perovskite particles, stoichiometric amounts of Fe(NO₃)₃·9H₂O (98%, Sigma-Aldrich), La(NO₃)₃·7H₂O (99.9%, Sigma-Aldrich), Sr(NO₃)₂ (99%, Noah chemical) were dissolved in deionized water at 30 °C and stirred for 30 min. Citric acid was then added by 3 times of total moles of metal ions in the solution. Two solutions were mixed with each other and stirred at 50 °C for 60 min. During the stirring, the mixed solution was heated to 80 °C and ethylene glycol was added to the solution to form a gel. The molar ratio of ethylene glycol to citric acid was 2:1. The solution was stirred at 80 °C for 120 min. To remove volatile components, the gel was subject to calcination in a furnace at 400 °C for 2 h with an air flow of 50 mL min⁻¹. The fur-

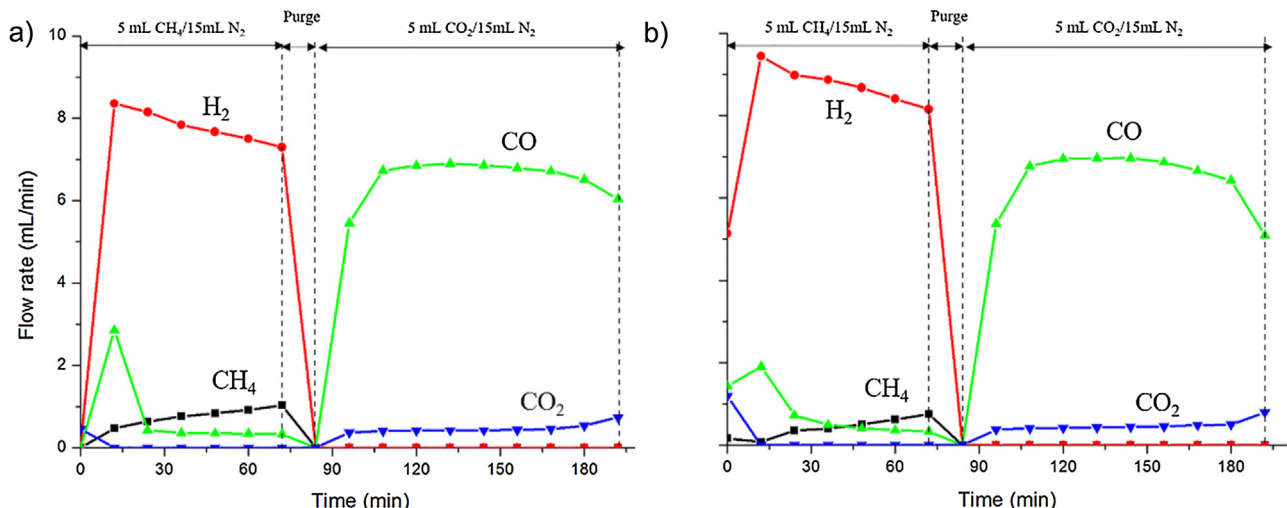


Fig. 3. Gas evolution profiles of CO₂-CLRD process with the fresh particle (a) and the 10-cycle spent particle (b).

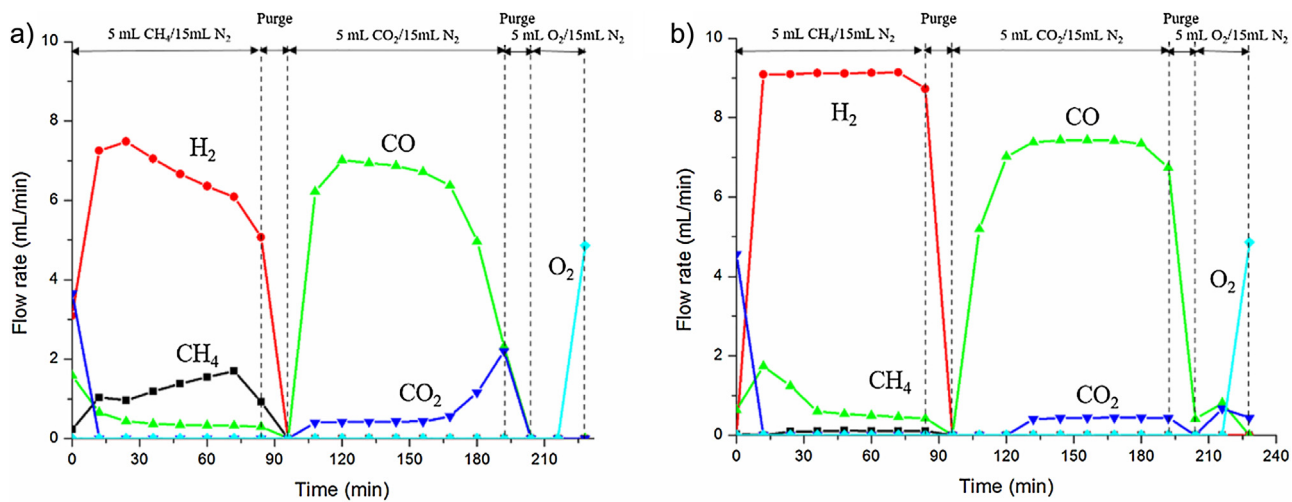


Fig. 4. Gas evolution profiles of CLRD process with combined CO_2 and O_2 oxidation with the fresh particle (a) and the 10-cycle spent particle (b).

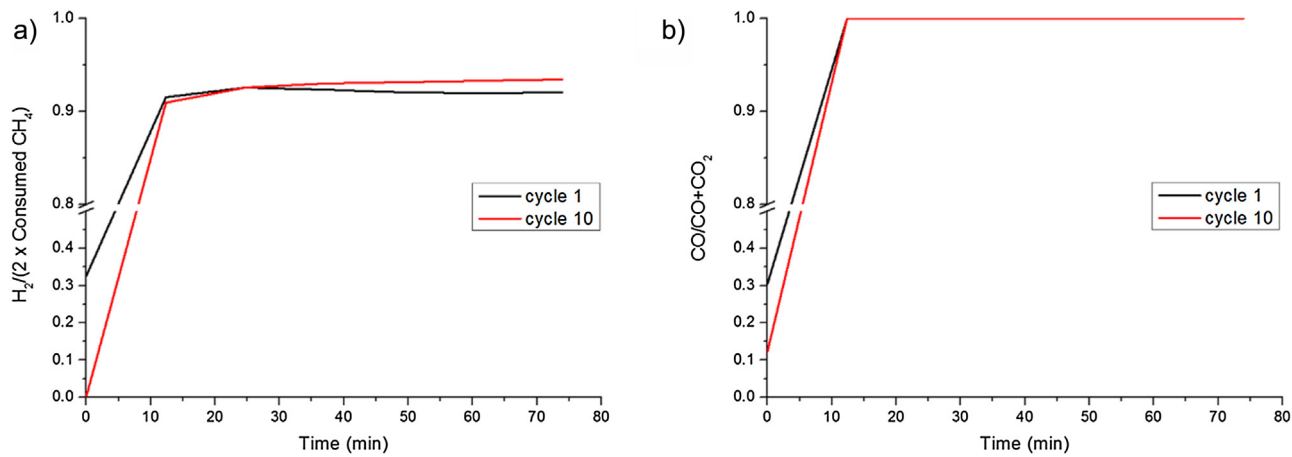


Fig. 5. Selectivity change of each syngas during comb-CLRD process. For H_2 (a) and CO (b).

nace was then heated to 800°C at a rate of 5°C min^{-1} and the gel was annealed with the same air flow for additional 4 h.

2.2. Characterization of perovskite particles

The composition of the crystal phase of both fresh and 10-cycle-spent particles (completely oxidized by O_2) analyzed by powder X-Ray Diffraction (XRD, RIGAKY, D/MAX-2500) and the samples were scanned continuously from 2° to 90° with a 0.01° resolution. The Jade program was used to process the data.

X-ray Photoelectron Spectroscopy (XPS) was used to analyze the surface composition (~ 10 nm in depth) of the fresh and 10-cycle spent particles. Up to $5.0 \mu\text{A}@4 \text{kV}$ of ion gun beam was operated to obtain depth profile data in the 10^{-10} torr ultra-high vacuum column. Using a Sigma probe with 0.47 eV of energy resolution, patterns of each element and composition ratios of surface were checked from 0 eV to 1350 eV . The data were processed in Avantage.

Field emission Transmission Electron Microscopy (FE-TEM) data were obtained to analyze the morphology of the particles. Working with energy-dispersive X-ray spectroscopy equipped on the FE-TEM, drift corrected spectrum image scanning was carried out for all components of the particle, La, Sr, Fe, Ni, and O.

A Temperature Programmed Reduction (TPR) was conducted through AutoChem II 2920 using H_2 as a reduction gas. 3 mL min^{-1} of H_2 was provided to the device in a balance with N_2 to make a total flow of 30 mL min^{-1} . With 1°C min^{-1} of heating rate, H_2

Table 1
 NiFe_2O_4 peak analysis of XRD signals (Unit: Å).

2θ	XS (Fresh)	XS (10-cycle)
30.290	308	622
35.663	325	611
43.393	233	444
63.022	183	499

Table 2
 $\text{La}_{0.8}\text{Sr}_{0.2}\text{FeO}_3$ peak analysis of XRD signals (Unit: Å).

2θ	XS (Fresh)	XS (10-cycle)
22.707	316	381
32.349	267	167
39.860	238	285
46.404	273	257
57.667	176	210
67.713	148	177
77.064	172	187

signals were analyzed once every 0.12 min until the temperature reached 900°C . The reducibility, thermal stability, and oxygen carrying capacity of both fresh and 10-cycle spent particles were investigated.

2.3. Redox reaction cycles

Reduction and oxidation reactions were conducted in a fixed bed reactor with an inner diameter of 9.8 mm at 1 atm. 300 mg of catalytic particles were packed in the reactor and surrounded with quartz wools. The reactor was heated with 15 mL min^{-1} of N_2 flow at a heating rate of 5°C min^{-1} until the temperature reached 900°C .

The CLRD process with O_2 oxidation ($\text{O}_2\text{-CLRD}$ in Fig. 1(a)) was started by introducing 5 mL min^{-1} of CH_4 and 15 mL min^{-1} of N_2 to the reactor for 72 min, followed by a purge step with only N_2 for 24 min. 5 mL min^{-1} of O_2 was then injected to the reactor to oxidize the catalytic particle and remove coke from the particle for 60 min. After another N_2 purge for 24 min, all of the previous steps were repeated per each cycle.

O_2 was replaced by CO_2 in the CLRD process with CO_2 oxidation ($\text{CO}_2\text{-CLRD}$), as presented in Fig. 1(b). After the same period of CH_4 reduction/decomposition and purge steps as in the $\text{O}_2\text{-CLRD}$, 5 mL min^{-1} of CO_2 was then provided to the reactor for the partial oxygen recovery and coke removal for 84 min. The next cycle was repeated after 24 min of the N_2 purge step.

The modified CLRD process with combined CO_2 & O_2 oxidation is shown in Fig. 1(c) (comb-CLRD). The CH_4 reduction/decomposition and N_2 purge steps proceeded in the same manner as in the two prior processes. The CO_2 oxidation/coke removal step was carried out for 84 min, followed by 24 min of the additional N_2 purge step in the same gas flow rate as in the previous cases. 5 mL min^{-1} of O_2 was then injected to the reactor to remove a small leftover of coke, also followed by 24 min of the additional N_2 purge step.

All of the three different processes conducted 10 cycles. All outlet gases of each process were analyzed with an online gas chromatograph (Agilent, 7890B) equipped with a thermal conductivity detector (TCD), using helium as a carrier gas. CO_2 was detected through a porapak Q column and other gases, CH_4 , H_2 , CO , and O_2 were analyzed through a molecular sieve 5A column.

3. Results and discussion

Three of our proposed CLRD processes demonstrated the stable operation of 10 cycles for 30 h. We investigated whether these processes are feasible to operate by maintaining the activity and stability of the synthesized catalytic particle as an efficient and stable oxygen carrier for chemical looping. It was remarkable that both methane conversion and syngas yield increased over the repeated cycles, which was closely related to the phase transition of biphasic $\text{Fe}_2\text{O}_3\text{-NiO}$ core to single-phase NiFe_2O_4 core in the perovskite particle.

3.1. CLRD with O_2 oxidation ($\text{O}_2\text{-CLRD}$)

An $\text{O}_2\text{-CLRD}$ cycle was conducted with the synthesized catalytic particle as an oxygen carrier for the chemical looping process. The performance of the fresh and the 10-cycle spent particles is shown in Fig. 2. During the CH_4 reduction step, CH_4 was partially oxidized and the products of CO and H_2 were mainly evolved. A small

Table 3
Detailed information of $\text{H}_2\text{-TPR}$ patterns.

Sample	Peak Temperature ($^\circ\text{C}$)	H_2 Consumed (moles of H_2/mol of Particle)
Fresh	292.5	0.03
	523.1	2.36
	902.3	0.42
10-cycle	556.7	2.71
	901.9	0.26

amount of CO_2 was generated at the early stage of the step because of sufficient lattice oxygen in the particles.

The ratio of CO to CO_2 continuously rose with the decrease of oxygen in the catalytic particle because the decreased lattice oxygen can prevent the full combustion but lead to the partial oxidation. After the production of CO_2 was ended in the CH_4 reduction step, the ratio of H_2/CO was much larger than 2 that is the stoichiometric ratio of POM. This indicates that parts of CH_4 were decomposed (not totally oxidized) to H_2 and carbon, and carbon deposits were formed on the surface of the particle. In the O_2 oxidation step, O_2 in the supplied air was completely consumed for both particle oxidation and removal of carbon deposits until the detected point of excess oxygen gas.

When the next CH_4 reduction step was repeated, it is striking that both conversion of CH_4 and total production rate of syngas slightly increased until the tenth cycle, as illustrated in Fig. 2(b) and Fig. S1 (refer to the Supplementary data). This may indicate that the lattice oxygen in the catalytic particle was fully regenerated with all the cokes removed at each cycle. Though the oxygen carrying capacity of the particle seemed to increase over the cycle, the production of CO_2 from the O_2 oxidation step was not dominant because the limitation in the oxygen transfer from the bulky metal

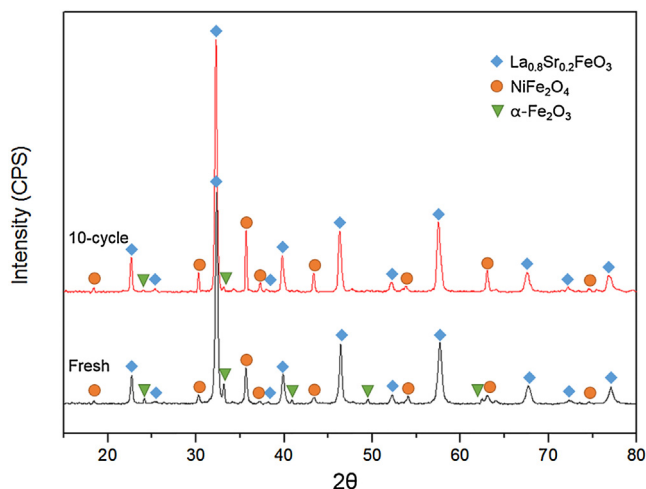


Fig. 6. XRD patterns of fresh and 10-cycle spent particle.

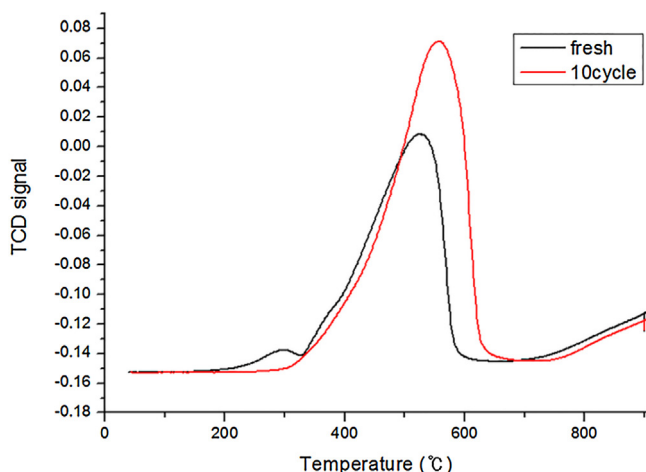


Fig. 7. TPR results of fresh and 10-cycle spent particle. TCD = Thermal Conductivity Detector.

oxide to the surface cannot lead to accelerating the transfer rate of lattice oxygen.

3.2. CLR modified CLR with CO₂ oxidation (CO₂-CLR)

The CO₂-CLR process switched the oxidizing gas from O₂ to CO₂ and its cycle operation was also performed to check the efficiency of oxidation and coke removal by CO₂, which eventually leads to the conversion of CO₂ to CO. In Fig. 3, both CH₄ conversion and H₂ production rate were increased over the redox cycle. The continuous improvement of CH₄ conversion and H₂ production also existed during the CH₄ reduction and decomposition step (refer to Fig. S2 in the Supplementary data). These results may indicate that using CO₂ as an oxidizer can also improve the redox ability of the catalytic particle in the same manner as in the O₂-CLR.

In the CO₂ oxidation step, most of CO₂ was converted with the production of CO and the complete removal of the coke generated from the decomposition of CH₄. Since there was no deactivation for all of the cycles, it seemed that the catalytic particle surface was completely recovered to the fresh state after the CO₂ oxidation step. The CO production rate and CO₂ conversion at the CO₂ oxidation step (Fig. S2(c)) were also improved over the redox cycle because more carbons were generated due to the increased CH₄ conversion and they were completely reacted with CO₂. Compared to the O₂-CLR process (Fig. 2), CO₂ production at the early stage of the CH₄ reduction step was much less and CO production was increasing in the CO₂-CLR process (Fig. 3) because the generated CO₂ can be reacted with the remaining coke for CO production and a small amount of CO₂ can also be reacted with the reduced metal.

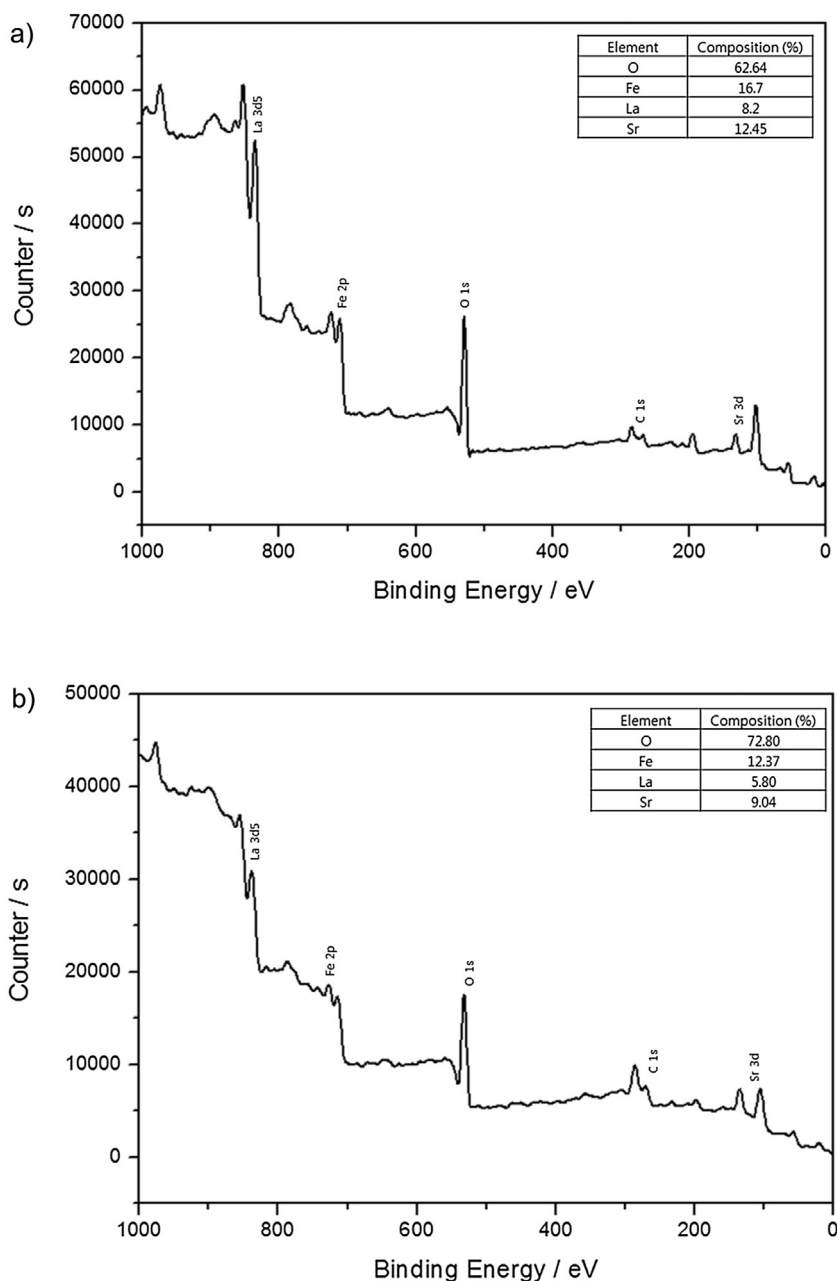


Fig. 8. XPS survey spectrum of fresh (a) and 10-cycle spent (b) particle.

3.3. Modified CLRD with combined CO₂ & O₂ oxidation (comb-CLRD)

The results of the comb-CLRD cycle test (Fig. 1(c)) with sequential CO₂ and O₂ oxidation, through 10 cycles, are shown in Fig. 4. In the CH₄ reduction and decomposition step, CH₄ consistently produced H₂ and CO for 72 min simultaneously with the generation of cokes. Most cokes were removed at the CO₂ oxidation step and the reduced particles were partially oxidized in this step. After observing a sudden drop of CO₂ conversion, the inlet gas was switched into O₂ and the catalytic particle was fully replenished with its consumed oxygen while remaining cokes were being removed. Since CO₂ gasified most of cokes and regenerated small amounts of lattice oxygen, a required amount of O₂ (0.2 L/g particle) to fully recover the lattice oxygen of the particle decreased to 20%, compared with that in the O₂-CLRD process (1.0 L/g particle). After finishing all cycles include N₂ purges, the CH₄ reduction/decomposition step started for the next cycle. Oxygen carrying capacity of the particle was improved over the cycle; therefore, both CH₄ conversion and syngas production rate were increased compared to the previous cycle (refer to Fig. 4 and Fig. S3 in the Supplementary data). Rising conversion of CH₄ leads to more formation of coke and H₂. In the CO₂ oxidation step, more CO₂ was reacted with coke than in the previous cycle.

3.4. Selectivity studies

If we focus on the selectivity of CO and H₂ production, the following four reactions primarily occur in the CH₄ reduction step for all of three CLRD processes (MO = metal oxide).



Based on these reactions, the selectivity toward all components of syngas from the comb-CLRD process at the first & the tenth cycle during the CH₄ reduction and decomposition step was analyzed with GC results and the results are indicated in Fig. 5.

At the beginning of the CH₄ reduction step, reaction (4) mainly occurred because the sufficient supply of lattice oxygen in the catalytic particle led to full oxidation of CH₄ to CO₂ and both selectivity toward H₂ and CO were low. However, after 12 min of the reduction step, the process was dominated by the syngas generation reaction (5) and the syngas selectivity was drastically increased as shown in Fig. 5. During this period, H₂ selectivity based on the consumed flow rate of CH₄ feed was maintained above 93% over 1 h and higher CO selectivity, close to 100% was observed. It appears that since the reverse shift reaction might take place (CO₂ + H₂ ↔ CO + H₂O) at a

high reaction temperature like 900 °C, CO₂ and H₂ were consumed for the formation of CO and thus, the H₂ selectivity is lower than the CO selectivity. However, the H₂ selectivity was slightly increased from average 92% at cycle 1 to above 93% at cycle 10 through the cyclic redox because the transition to the single phase of NiFe₂O₄, which will be shown in the subsequent sections, may lead to better reaction selectivity for syngas production.

3.5. Effects of the core phase change on enhanced catalytic particle activity and stability

The crystalline structures of both fresh and 10-cycle-spent catalytic particles analyzed in XRD were shown in Fig. 6. The XRD pattern of the fresh particle presented the well-formed perovskites structures and the existence of both hematite (α-Fe₂O₃) and NiFe₂O₄. Before the calcination of the Fe₂O₃-NiO mixture, however, the peaks were only matched with maghemite (γ-Fe₂O₃) and not with crystalline NiO (refer to Fig. S4 in the Supplementary data). This indicated that NiO was amorphous, parts of the Fe₂O₃ phase in the mixture are combined with the amorphous NiO and the rest of maghemite is changed to stable hematite during the calcination step for the preparation of the fresh particle. The pattern of the 10-cycle-spent particle shows that the structures of perovskites are maintained over the continuous redox cycle at the high temperature (900 °C). Most of the signals of hematite are weakened or disappear with the signals of NiFe₂O₄ intensified.

Xin et al. [42] studied the structural transformation of iron oxides through consecutive redox cycles and demonstrated that the stable hematite can be changed to the metastable maghemite. The relatively unstable phase of the maghemite can lead to easier formation of a single phase of NiFe₂O₄, which provides better redox kinetics. This phase change increased the activity of chemical looping process through the cyclic operation. The hematite portion diminished over the redox cycle and was combined with amorphous NiO to form NiFe₂O₄.

Table 1 indicated the crystallite size of the NiFe₂O₄ based on the Scherrer equation. Through 10-cycle experiments, the crystallite size of NiFe₂O₄ significantly increased with small changes in the size of the perovskites (Table 2), which means the integration of amorphous NiO with Fe₂O₃. Since the amorphous NiO was reacted and transitioned to crystalline NiFe₂O₄, it seems that the crystallinity of the catalytic particle increased during the continuous redox cycle. Thus, the increased crystallinity (Fig. 6) and crystallite size of the 10-cycle spent particle (Tables 1 and 2) can cause enhanced redox capability of the particle. Fig. 7 portrayed the H₂-TPR analyzed curves of fresh and the 10-cycle-spent particle. In the pattern of the fresh particle, three major peaks were detected at 292.5 °C, 523.1 °C, and 902.3 °C. However, in the 10-cycle spent particle, the first two peaks were combined and moved to the higher temperature. The different patterns of the two curves were caused by the phase change of the particle, which was already demon-

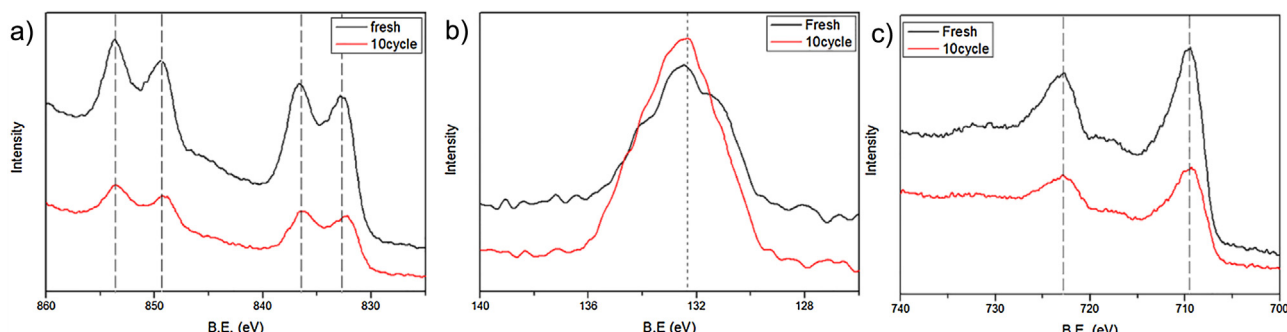


Fig. 9. XPS spectrum of La 3d (a), Sr 3d (b) and Fe 2p (c) of fresh and 10-cycle spent particle.

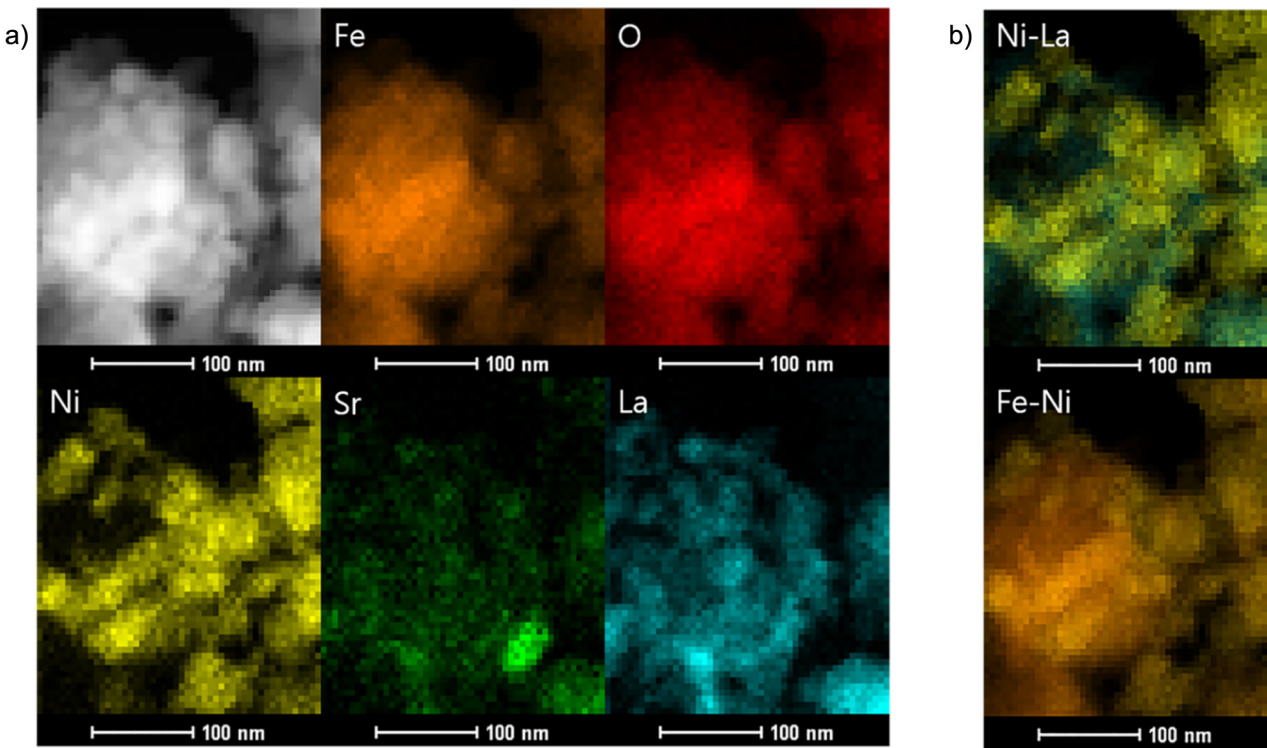


Fig. 10. EFTEM mappings of all elements (Fe, O, Ni, Sr, La) (a) and binary elemental mapping (b).

strated in the XRD analysis (Fig. 6). Both merging two peaks and increasing initial desorption temperature indicated that the stability of particles was improved over the repeated cycle. Wider area of the curve in the spent particle than the fresh particle (Fig. 7) can indicate the increased oxygen carrying capacity of particles as also shown in the H₂-TPR result (Table 3). Compared with the fresh particle, the largest peak temperature moved from 523.1 °C to 556.7 °C and the total H₂ oxidizing ability increased by 5.5%. Both enhanced thermal stability and oxygen mobility can lead to the sustainable CH₄ reduction/decomposition and CO₂ & O₂ sequential oxidation steps for improving the H₂ and CO production.

3.6. Composition and morphology

The near-surface composition and the binding energy of both fresh and 10-cycle-spent catalytic particles from XPS analyses revealed that all of the elements of La, Sr, Fe, and O existing in the perovskite (La_{0.8}Sr_{0.2}FeO₃) were detected on the surface while there was no observation of Ni on the outer surface of both fresh and 10-cycle-spent particles as shown in Fig. 8. Thus, it can be conjectured that Ni is located in the core phase of the particle. The spectra of La 3d, Sr 3d and Fe 2p of fresh and spent particles were illustrated in Fig. 9. The shapes of these peaks were similar to the peak shape of La_{0.8}Sr_{0.2}FeO₃ perovskites reported in the prior studies [34,43–45] and maintained after the ten redox cycles, which means that the structure of perovskites has been unaltered over the repeated cycle.

The EFTEM mapping of each element in the catalytic particle also supports the formation of the partial core-shell structure, as illustrated in Fig. 10. Since the particle mainly consists of NiFe₂O₄ and La_{0.8}Sr_{0.2}FeO₃, both Fe and O elements are homogeneously distributed over all the areas of the particle as shown in Fig. 10(a). The two mappings of La and Sr elements were similar to each other and those are mainly located on the surface area. Most of Ni atoms were concentrated inside of the particle because both mappings of La and Fe elements mostly overlaid the Ni element mapping

(Fig. 10(b)). Along with the near-surface composition identified from the XPS analysis, these can be an evidence to indicate that most of Ni atoms exist at the core of the particle while the other elements are dominantly found on the surface, forming the partial core-shell structure.

4. Conclusions

This work has investigated the activity, selectivity, and thermal stability of a Fe₂O₃–NiO/La_{0.8}Sr_{0.2}FeO₃ perovskite oxygen carrier for the methane Chemical Looping Reforming and Decomposition (CLRD) process combined with CO₂ conversion. The catalytic particle activity has been gradually improved and the conversion of CH₄ showed 97% for 72 min per cycle over the repeated ten cycles. The structure of the perovskite remained stable over the redox cycles. Adding NiO to Fe₂O₃ led to the formation of NiFe₂O₄, which could further increase crystallinity to enhance both oxygen carrying capacity and particle's catalytic activity. CO₂ can replace O₂ for the coke removal on the surface of the particle and it showed above 90% of CO₂ conversion to CO over 84 min during the particle oxidation step by CO₂. The combined oxidation by CO₂ and O₂ was effective to increase the syngas production rate. These results have demonstrated that the CLRD process with combined CO₂ & O₂ oxidation is a promising alternative process for simultaneous methane reforming and CO₂ conversion.

Acknowledgements

The authors are grateful for the financial support from the Mid-career Researcher Program and the UK-Korea Joint Research Program, through NRF grants (2014R1A2A2A01007076 and 2015M2A7A1000219) funded by the Ministry of Science, ICT, and Future Planning.

Appendix A. Supplementary data

Supplementary data associated with this article can be found, in the online version, at <http://dx.doi.org/10.1016/j.apcatb.2016.09.020>.

References

- [1] B. Bao, M.M. El-Halwagi, N.O. Elbashir, *Fuel Process. Technol.* 91 (2010) 703–713.
- [2] J.A. Elia, R.C. Baliban, X. Xiao, C.A. Floudas, *Comput. Chem. Eng.* 35 (2011) 1399–1430.
- [3] M.R. Rahimpour, A. Mirvakili, K. Paymooni, *Energy* 36 (2011) 1223–1235.
- [4] S.H. Hu, B.W. Wang, Y.J. Lv, W.J. Yan, *Plasma Sci. Technol.* 15 (2013) 555–561.
- [5] M.M. Moshrefi, F. Rashidi, H.R. Bozorgzadeh, S.M. Zekordi, *Plasma Chem. Plasma Process.* 32 (2012) 1157–1168.
- [6] S. Motozuka, M. Tagaya, T. Ikoma, M. Morinaga, T. Yoshioka, J. Tanaka, *J. Phys. Chem. C* 117 (2013) 16104–16118.
- [7] G.D. Nuernberg, H.V. Fajardo, E.L. Foletto, S.M. Hickel-Probst, N.L.V. Carreno, L.F.D. Probst, J. Barrault, *Catal. Today* 176 (2011) 465–469.
- [8] A.M. Zhu, *Abstr. Pap. Am. Chem. Soc.* 235 (2008).
- [9] L. Barelli, G. Bidini, F. Gallorini, S. Servili, *Energy* 33 (2008) 554–570.
- [10] C. Zhao, Z. Zhou, Z. Cheng, X. Fang, *Appl. Catal. B: Environ.* 196 (2016) 16–26.
- [11] V. Kyriakou, I. Garagounis, A. Vourros, E. Vasileiou, A. Manerbino, W.G. Coors, M. Stoukides, *Appl. Catal. B—Environ.* 186 (2016) 1–9.
- [12] O. Muraza, A. Galadima, *Int. J. Energy Res.* 39 (2015) 1196–1216.
- [13] J.S. Zhang, F.X. Li, *Appl. Catal. B—Environ.* 176 (2015) 513–521.
- [14] Z.F. Bian, I.Y. Suryawinata, S. Kawi, *Appl. Catal. B—Environ.* 195 (2016) 1–8.
- [15] B.C. Enger, R. Lodeng, A. Holmen, *Appl. Catal. A—Gen.* 346 (2008) 1–27.
- [16] Z. Boukha, C. Jiménez-González, M. Gil-Calvo, B. de Rivas, J.R. González-Velasco, J.I. Gutiérrez-Ortiz, R. López-Fonseca, *Appl. Catal. B: Environ.* 199 (2016) 372–383.
- [17] G. Pantaleo, V. La Parola, F. Deganello, R.K. Singha, R. Bal, A.M. Venezia, *Appl. Catal. B—Environ.* 189 (2016) 233–241.
- [18] M.C. Tang, L. Xu, M.H. Fan, *Appl. Energy* 151 (2015) 143–156.
- [19] J. Adanez, A. Abad, F. Garcia-Labiano, P. Gayan, L.F. de Diego, *Prog. Energy Combust.* 38 (2012) 215–282.
- [20] M. Ryden, A. Lyngfelt, T. Mattisson, *Energ. Fuel* 22 (2008) 2585–2597.
- [21] P. Chiesa, G. Lozza, A. Malandrino, M. Romano, V. Piccolo, *Int. J. Hydrogen Energy* 33 (2008) 2233–2245.
- [22] M. Ortiz, A. Abad, L.F. de Diego, F. Garcia-Labiano, F. Gayan, J. Adanez, *Int. J. Hydrogen Energy* 36 (2011) 9663–9672.
- [23] M. Ryden, P. Ramos, *Fuel Process. Technol.* 96 (2012) 27–36.
- [24] L. Silvester, A. Antzara, G. Boskovic, E. Heracleous, A.A. Lemonidou, D.B. Bukur, *Int. J. Hydrogen Energy* 40 (2015) 7490–7501.
- [25] Z.Q. Zhou, L. Han, G.M. Bollas, *Int. J. Hydrogen Energy* 39 (2014) 8535–8556.
- [26] D. Kang, J.W. Lee, *Appl. Catal. B—Environ.* 186 (2016) 41–55.
- [27] S.Y. Chen, Z.P. Xue, D. Wang, W.G. Xiang, *J. Power Sources* 215 (2012) 89–98.
- [28] L.F. de Diego, M. Ortiz, J. Adanez, F. García-Labiano, A. Abad, P. Gayan, *Chem. Eng. J.* 144 (2008) 289–298.
- [29] M. Johansson, T. Mattisson, A. Lyngfelt, A. Abad, *Fuel* 87 (2008) 988–1001.
- [30] A. Edrisi, Z. Mansoori, B. Dabir, A. Shahnazari, *Int. J. Hydrogen Energy* 39 (2014) 10380–10391.
- [31] Q.J. Guo, Y. Cheng, Y.Z. Liu, W.H. Jia, H.J. Ryu, *Ind. Eng. Chem. Res.* 53 (2014) 78–86.
- [32] F. Liu, L.Y. Chen, J.K. Neathery, K. Saito, K.L. Liu, *Ind. Eng. Chem. Res.* 53 (2014) 16341–16348.
- [33] G.Q. Wei, F. He, Z. Huang, K. Zhao, A.Q. Zheng, H.B. Li, *Chin. J. Chem.* 32 (2014) 1271–1280.
- [34] L.M. Neal, A. Shafiefarhood, F.X. Li, *ACS Catal.* 4 (2014) 3560–3569.
- [35] R. Siriwardane, H.J. Tian, J. Fisher, *Int. J. Hydrogen Energy* 40 (2015) 1698–1708.
- [36] S. Bhavsar, M. Najera, G. Veser, *Chem. Eng. Technol.* 35 (2012) 1281–1290.
- [37] V.V. Galvita, H. Poelman, G.B. Marin, *J. Power Sources* 286 (2015) 362–370.
- [38] M. Najera, R. Solunke, T. Gardner, G. Veser, *Chem. Eng. Res. Des.* 89 (2011) 1533–1543.
- [39] V.V. Galvita, H. Poelman, C. Detavernier, G.B. Marin, *Appl. Catal. B—Environ.* 164 (2015) 184–191.
- [40] J. Hu, L. Buelens, S.-A. Theofanidis, V.V. Galvita, H. Poelman, G.B. Marin, *J. CO₂ Util.* 16 (2016) 8–16.
- [41] Y.L. Kuo, W.M. Hsu, P.C. Chiu, Y.H. Tseng, Y. Ku, *Ceram. Int.* 39 (2013) 5459–5465.
- [42] X. Zhang, Y.G. Niu, X.D. Meng, Y. Li, J.P. Zhao, *CrystEngComm* 15 (2013) 8166–8172.
- [43] A. Shafiefarhood, N. Galinsky, Y. Huang, Y.G. Chen, F.X. Li, *ChemCatChem* 6 (2014) 790–799.
- [44] X. Montero, W. Fischer, F. Tietz, D. Stover, M. Cassir, I. Villarreal, *Solid State Ionics* 180 (2009) 731–737.
- [45] K.L. da Silva, A. Borger, K.D. Becker, F. Tietz, D. Stover, *Solid State Ionics* 192 (2011) 552–556.